

Possibility of an unconventional spin state of Ir⁴⁺ in Ba₂₁Ir₉O₄₃ single crystal

L. Yang,^{1,2} M. Jeong,² A. Arakcheeva,¹ I. Živković,² B. Náfrádi,¹ A. Magrez,³ A. Pisoni,¹ J. Jacimovic,¹ V. M. Katukuri,⁴ S. Katrych,¹ N. E. Shaik,² O. V. Yazyev,⁴ L. Forró,¹ and H. M. Rønnow^{2,*}

¹Laboratory of Physics of Complex Matter, Institute of Physics,

Ecole Polytechnique Fédérale de Lausanne (EPFL), CH-1015 Lausanne, Switzerland

²Laboratory for Quantum Magnetism, Institute of Physics,

Ecole Polytechnique Fédérale de Lausanne (EPFL), CH-1015 Lausanne, Switzerland

³Crystal Growth Facility, Institute of Physics, Ecole Polytechnique Fédérale de Lausanne (EPFL), CH-1015 Lausanne, Switzerland

⁴Institute of Physics, Ecole Polytechnique Fédérale de Lausanne (EPFL), CH-1015 Lausanne, Switzerland

(Received 9 June 2016; revised manuscript received 9 August 2016; published 6 September 2016)

We report the synthesis of single crystals of a novel layered iridate Ba₂₁Ir₉O₄₃ and present the crystallographic, transport, and magnetic properties of this material. The compound has a hexagonal structure with two iridium oxide layers stacked along the *c* direction. One layer consists of a triangular arrangement of Ir₂O₉ dimers while the other layer comprises two regular octahedra and one triangular pyramid, forming interpenetrated triangular lattices. The resistivity as a function of temperature exhibits an insulating behavior, with a peculiar T^{-3} behavior. Magnetic susceptibility shows antiferromagnetic Curie-Weiss behavior with $\Theta_{\text{CW}} \simeq -90$ K while a magnetic transition occurs at a substantially lower temperature of 9 K. We discuss possible valence states and effective magnetic moments on Ir ions in different local environments and argue that the Ir ions in a unique triangular-pyramidal configuration likely carry unusually large magnetic moments.

DOI: [10.1103/PhysRevB.94.104403](https://doi.org/10.1103/PhysRevB.94.104403)

There is considerable interest in studying correlated 5*d*-electron transition metal oxides with strong spin-orbit coupling (SOC) [1–3]. Recent focus has been on new iridate compounds where experimental discoveries have strongly challenged theoretical predictions. For example, in pentavalent (Ir⁵⁺) 5*d*⁴ iridates a strong SOC is predicted to realize a nonmagnetic $J = 0$ state [4], but substantial magnetic moments have been found in Ba₂YIrO₆ [5] and especially in Sr₂YIrO₆ [6], where structural distortion of the octahedral environment leads to 0.91 μ_{B}/Ir . Furthermore, a possible realization of a spin-orbital liquid with Ir⁵⁺ has been discussed for 6*H* hexagonal Ba₃ZnIr₂O₉ powder [7].

In tetravalent (Ir⁴⁺) 5*d*⁵ iridates, such as Sr₂IrO₄ [8–10], a complex spin-orbit entangled $J_{\text{eff}} = 1/2$ state is realized, with a reduced bandwidth due to the splitting from the $J_{\text{eff}} = 3/2$ states, which leads to the localization of electrons even by a relatively small on-site Coulomb interaction compared to their 3*d* counterparts. Additional effects of SOC include *XY* anisotropy [11,12], locking of the magnetic moment to the correlated rotation of oxygen octahedra in Sr₂IrO₄ [13], anisotropic dimer excitations in Sr₃Ir₂O₇ [14], and Kitaev-type magnetic interactions in Na₂IrO₃ [15]. Structural distortions from the ideal octahedral environment have been observed in the pyrochlore family of the type $R_2\text{Ir}_2\text{O}_7$ (R = rare earth) where trigonal compression induces a reconstruction of energy levels [16,17].

So far, to the best of our knowledge, there have been very few reports [18] of oxides containing Ir⁴⁺ or Ir⁵⁺ ions in an environment different from octahedral. Following the observations of profound influence of structural effects onto the energy scheme of iridium ions and consequently the resulting spin-orbital state, it can be expected that nonoctahedral ligand coordination could result in different properties.

Here we report the synthesis, crystal structure, transport, and magnetic properties of single crystals of a layered iridate Ba₂₁Ir₉O₄₃. It consists of layers of a triangular lattice of Ir₂O₉ dimers, much like in Ba₃ZnIr₂O₉, that are intercalated by another layer of a triangular lattice containing three different iridium environments: two regular octahedra and a triangular pyramid [see Figs. 1(a)–1(c) for the structure]. We conclude that the triangular pyramid represents a novel environment for an Ir⁴⁺ ion with the high-spin state $J_{\text{eff}} = 5/2$.

Single crystals of Ba₂₁Ir₉O₄₃ were grown in two steps. First, a mixture of powders with the molar ratio of BaCO₃ : IrO₂ = 13 : 2 was heated for 2 days at 1000 °C and cooled down slowly (2 °C/h) to 700 °C in an Al₂O₃ crucible. After the reaction, black powder was obtained and pressed into a pellet. Second, the mixture of the weight ratio of the pellet : K₂CO₃ powder flux = 1 : 20 was heated for 2 days at 1150 °C and cooled down to 800 °C at 2 °C/h in an Al₂O₃ crucible. Black-colored single crystals of Ba₂₁Ir₉O₄₃ with a platelike shape were obtained after the reaction, as shown in Fig. 1(d), where the maximum dimensions were 2 × 2 × 0.1 mm³. The direction perpendicular to the plate coincides with the crystallographic *c* axis of the hexagonal system. The chemical composition was determined using an energy dispersive x-ray detector (EDX, Oxford Instruments EDX X-MAX), which yielded the molar ratios Ba : Ir of 69.5(4) : 30.6(7).

Single-crystal x-ray diffraction data were collected at room temperature using a SuperNova diffractometer equipped with a CCD detector and a high-intensity microfocus x-ray source (Mo $K\alpha$ radiation). Data reduction and analytical absorption correction were done using CRYCALISPRO software [19]. The crystal structure was solved by the SUPERFLIP algorithm [20] and refined using JANA2006 [21]. Resistivity was measured on a single plate of crystal using a standard four-probe configuration with dc current. Bulk magnetic measurements were performed using a superconducting quantum interference device (SQUID) magnetometer. A dozen plate-like crystals

*henrik.ronnow@epfl.ch

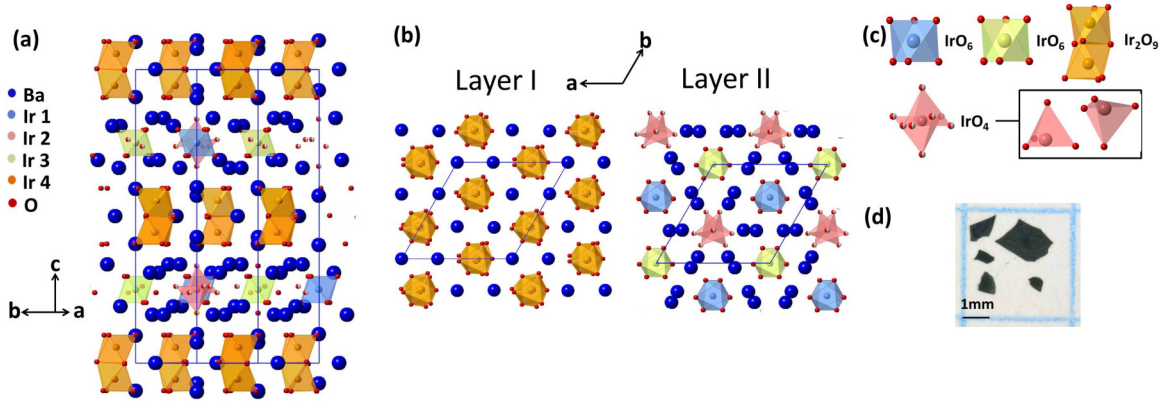


FIG. 1. (a) Crystal structure of $\text{Ba}_{21}\text{Ir}_9\text{O}_{43}$ where a unit cell is drawn by a solid line. (b) Two different layers of triangular lattice Ir-O polyhedra, labeled as Layer I $[\text{Ba}_9\text{Ir}_6\text{O}_{27}]^{-6}$ (left) and Layer II $[\text{Ba}_{12}\text{Ir}_3\text{O}_{16}]^{+6}$ (right). (c) The Ir-O polyhedra: blue and green IrO_6 octahedra are geometrically identical within one standard deviation; face-sharing orange octahedra form a Ir_2O_9 dimer; red polyhedron is shown as a statistical superposition of two possible IrO_4 triangular pyramids, having the same geometry but opposite in orientation along the c direction, with 50% occupancy on every oxygen site. (d) Representative single crystals of $\text{Ba}_{21}\text{Ir}_9\text{O}_{43}$.

with total mass of 9.4 mg were stacked with a common c axis but random orientation in their ab plane. Electron spin resonance (ESR) measurements were performed on the stacked crystals using a Bruker Elexys E500 continuous-wave spectrometer at 9.4 GHz, equipped with a He-gas flow cryostat.

Figure 1(a) shows the crystal structure which belongs to the hexagonal system. The details of the data collection and structure refinement are listed in Table I, and further information is available in the Supplemental Material [22]. The structure consists of two different layered blocks. For Layer I, the central structural feature is the formation of Ir_2O_9 dimers composed of two face-sharing IrO_6 octahedra (Ir4), as shown in Figs. 1(b) and 1(c). Such dimers are typical for $6H$ -perovskite-type oxides [23,24]. Layer II consists of isolated IrO_6 octahedra (Ir1 and Ir3) and an IrO_4 triangular pyramid (Ir2). The IrO_4 pyramids appear in two possible orientations, that is, an apical oxygen pointing either upward or downward, in statistically equal distribution. The chemical formula $\text{Ba}_{21}\text{Ir}_9\text{O}_{43}$ was obtained from the fully occupied positions for all sites of all Ir atoms with the accuracy 1.00(1).

TABLE I. Details of the data collection and structure refinement for $\text{Ba}_{21}\text{Ir}_9\text{O}_{43}$ obtained at room temperature using Mo $K\alpha$ radiation with $\lambda = 0.71073\text{\AA}$.

Empirical formula	$\text{Ba}_{21}\text{Ir}_9\text{O}_{43}$
Formula weight (g/mol)	5302.07
Space group	$P6_322$
Unit cell parameters (\AA)	$a = b = 10.5102(9)$ $c = 25.1559(19)$
Volume (\AA^3)	2406.5
Z	2
Calculated density (g/cm^3)	7.317
Reflections collected/unique	6486/1188
Data/restraints/parameters	1188/0/81
Final R indices [$I > 3\sigma(I)$]	$R = 0.0629$, $wR = 0.0586$
Goodness-of-fit	1.46

The molar ratio of Ba/Ir from the formula $21/9 = 2.33$ is close to the value $69.5(4)/30.6(7) = 2.27(7)$ from the EDX analysis.

The electrical resistivity ρ as a function of temperature along the in-plane (ρ_{ab}) and the out-of-plane (ρ_c) directions is shown in Fig. 2. At room temperature the magnitudes are $\rho_{ab} = 60 \Omega\text{cm}$ and $\rho_c = 10^4 \Omega\text{cm}$, respectively. Both ρ_{ab} and ρ_c increase monotonically as temperature decreases, revealing

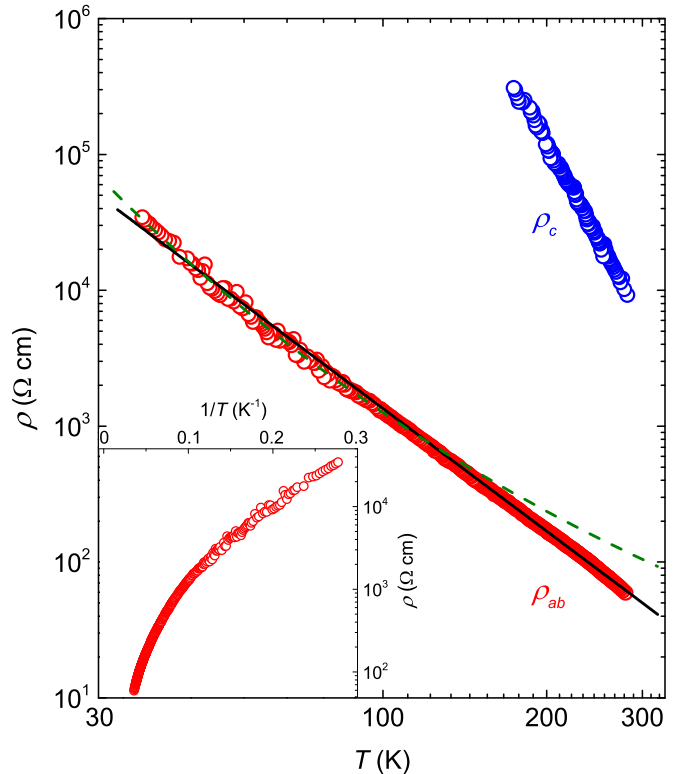


FIG. 2. Log-log plot of in-plane (ρ_{ab}) and out-of-plane (ρ_c) resistivity as a function of temperature where dashed and solid lines represent the two-dimensional VRH model and $\rho \propto T^{-3}$ behavior, respectively. Inset shows an Arrhenius plot of ρ_{ab} .

the insulating nature of this compound. ρ_c was measured only above 150 K due to high resistance.

The ρ_{ab} could not be fitted by a thermally activated exponential behavior, $\rho \propto \exp(E_a/k_B T)$, where E_a is an activation energy. This is evident from an Arrhenius plot shown in the inset of Fig. 2 where no linear regime is found. On the other hand, we note that the resistivity in a number of iridates such as $\text{Sr}_3\text{Ir}_2\text{O}_7$ [25], NaIrO_3 [26,27], Ba_2IrO_4 [28], and Sr_2IrO_4 [29] has been found to fit to a variable-range hopping (VRH) model. Indeed, the low-temperature resistivity below 120 K can be fitted to $\rho(T) = \rho_0 \exp(T_0/T)^{1/3}$, which is known as the two-dimensional VRH model, and the result is shown by the dashed line in Fig. 2. However, we also discover that ρ_{ab} follows remarkably well a power law such as $\rho_{ab} \propto T^{-3}$ as shown by the solid line in a log-log plot of Fig. 2. While this might be a coincidence, it could suggest that ρ is controlled by unconventional scaling. Results of Seebeck coefficient measurements are given in the Supplemental Material [22].

Figure 3(a) shows the inverse magnetic susceptibility $1/(M/H - \chi_0)$, where M is magnetization, as a function of temperature for the applied field $H = 1$ T parallel (square)

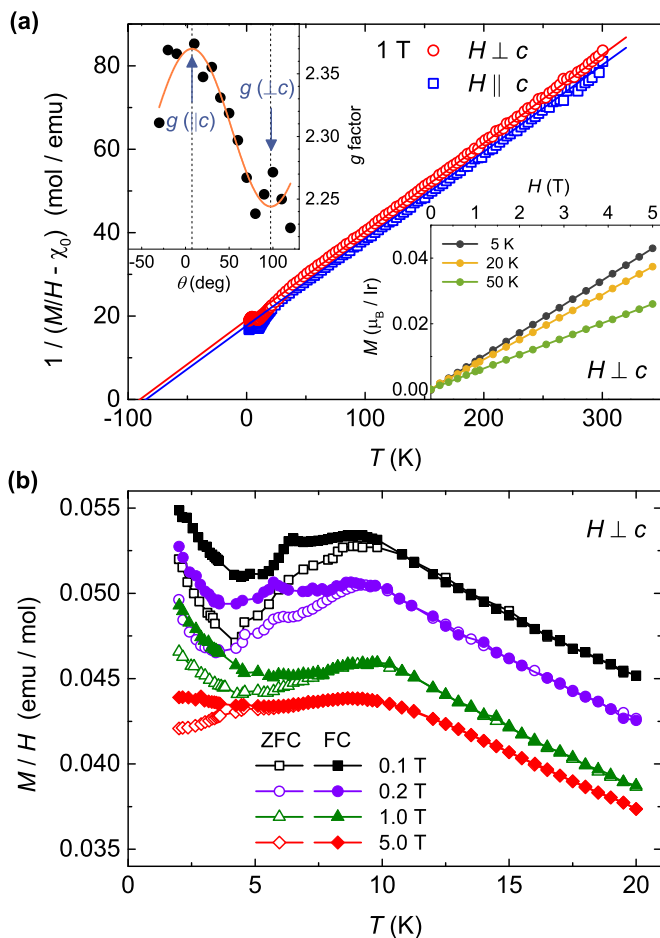


FIG. 3. (a) Inverse magnetic susceptibility $1/(M/H - \chi_0)$ versus temperature in $H = 1$ T applied perpendicular and parallel to the c axis, respectively. Lower-right inset: Isothermal magnetization as a function of field for different temperatures. Upper-left inset: Angular dependence of the g factor at room temperature. (b) The susceptibility as a function of temperature in various applied fields.

and perpendicular (circles) to the c axis. The high-temperature part follows Curie-Weiss behavior, as shown by the solid lines. Overall, the magnetic behavior appears qualitatively similar for both $H \parallel c$ and $H \perp c$. The lower-right inset of Fig. 3(a) shows the magnetization as a function of field for $H \perp c$ at different temperatures. The $M(H)$ curve becomes linear with H above 1.5 T in the measured temperature range.

The data above 100 K was fitted by a Curie-Weiss law, $\chi(T) = C/(T - \Theta_{\text{CW}}) + \chi_0$, yielding for $H \perp c$ the Curie constant $C = 4.72(9)$ emu/mol K, corresponding to the effective moment $\mu_{\text{eff}} = 2.05(2)\mu_B/\text{Ir}$, the Curie-Weiss temperature $\Theta_{\text{CW}} = -90(2)$ K, and the temperature-independent term $\chi_0 = -6.4 \times 10^{-3}$ emu/mol. For $H \parallel c$ the fit gave $C = 4.8(1)$ emu/mol K, $\mu_{\text{eff}} = 2.07(3)\mu_B/\text{Ir}$, $\Theta_{\text{CW}} = -85(3)$ K, and $\chi_0 = 1.2(3) \times 10^{-3}$ emu/mol. From the negative value of Θ_{CW} we infer that the dominant magnetic interaction is antiferromagnetic. The temperature-independent term χ_0 is rather large and anisotropic, but similar large and anisotropic values have been reported for other iridates, such as NaIrO_3 [26], $\text{Pr}_2\text{Ir}_2\text{O}_7$ [30], and $\text{Ba}_8\text{Al}_2\text{IrO}_{14}$ [31]. We encourage a theoretical scrutiny of these unusual χ_0 effects.

The low-temperature behavior of $\chi(T)$ in different fields is shown in Fig. 3(b). Most notably, a splitting for zero-field-cooled (ZFC) and field-cooled (FC) is observed below the 9 K maximum while the bifurcation point shifts to lower temperature as the field strength is increased, e.g., the ZFC and FC data split at 5 K in 5 T. An additional small peak is observed in the FC 0.1 and 0.2 T data around 6 K, which disappears in stronger fields.

At room temperature, a single paramagnetic ESR line was observed. The g factor and its anisotropy were obtained by recording the line position as the applied field orientation was varied with respect to the crystallographic axes. The upper-left inset of Fig. 3(a) shows the obtained g -factor anisotropy, which exhibits a characteristic $\cos^2 \theta$ angular dependence as the field orientation varies from $H \parallel c$ to $H \perp c$. The principal values of the g factor are found to be $g(\parallel c) = 2.37$ and $g(\perp c) = 2.24$. The g factor anisotropy in the ab plane was smaller than the ESR linewidth of 20 mT which gives an upper bound of 0.05 for the ab -plane anisotropy.

It is surprising that this compound displays an average effective moment of $2.1 \mu_B$, when similar compounds have been reported to exhibit effective moments from 0.2 to $1.3 \mu_B$ [7,32]. One possible scenario would be that all four iridium sites exhibit unusually high moments of $\sim 2 \mu_B$. Below we present another possible interpretation, which merits further experimental and theoretical consideration. Let us start by considering possible valence states for the different iridium environments in $\text{Ba}_{21}\text{Ir}_9\text{O}_{43}$. The most common valence states for Ir ions in oxides are Ir^{3+} , Ir^{4+} , Ir^{5+} , and Ir^{6+} , which may apply to Ir1, Ir2, and Ir3 sites. For the Ir4 sites with the dimers of face-sharing octahedra, one can make reference to the data from a large family of $\text{Ba}_3M\text{Ir}_2\text{O}_9$, where $M = \text{Mg}, \text{Ca}, \text{Sc}, \text{Ti}, \text{Zn}, \text{Sr}, \text{Zr}, \text{Cd}, \text{and In}$ [7,32], which have structurally very similar dimer units. In this family, a systematic relation is found between the valence state and Ir-Ir as well as Ir-O distances of the face-sharing octahedra, i.e., larger Ir-Ir and smaller Ir-O distances for higher valence states [32]. For instance, the Ir^{5+} states are stabilized in $\text{Ba}_3\text{ZnIr}_2\text{O}_9$ with the Ir-Ir distance of 2.75 Å, and similarly for others with $M = \text{Mg}, \text{Cd}, \text{and Sr}$

TABLE II. Valence states in octahedral and triangular pyramid environments for the different Ir ions.

	Ir1	Ir2	Ir3	Ir4
A	3+	5+	6+	5+
B	5+	4+	5+	5+
C	4+	6+	4+	5+

[7,32]. The very similar Ir-Ir distance of 2.74 Å in Ba₂₁Ir₉O₄₃ indicates that Ir⁵⁺ states are realized on Ir4 sites.

Next we can list possible valence states for Ir ions by imposing the charge neutrality condition for the overall system. For the given chemical formula Ba₂₁Ir₉O₄₃, we find that only three valence configurations are possible [22], which are listed in Table II. For the two regular octahedral sites, Ir1 and Ir3, it is found that their Ir-O distances are very similar, 1.95(3) Å and 1.90(3) Å, respectively. This indicates that they likely adopt the same valence state, excluding the combination A. To discriminate between combinations B and C, we consider the charge balance within the Layer II. As can be seen from Fig. 1, there are no shared oxygens between neighboring iridium ions within a layer, with Ba²⁺ ions being found between Ir-O clusters. For B the charge on octahedral units (IrO₆ clusters) is $Q_{\text{oct}}^{\text{B}} = -7$, while on a triangular pyramid (IrO₄ cluster) it is $Q_{\text{pyr}}^{\text{B}} = -4$ [33]. However, for C these values become much more disproportionate, $Q_{\text{oct}}^{\text{C}} = -8$ and $Q_{\text{pyr}}^{\text{C}} = -2$, which appears rather unlikely. Therefore, we conclude that the combination B is the most likely valence configuration.

We can now turn our attention to the consideration of magnetic moments residing on individual iridium sites. The values of effective moments for the case B, for instance, are calculated by using

$$(\mu_{\text{eff}}/\mu_{\text{B}})^2 N_{\text{Ir}} = \mu_{\text{pyr}}^2 N_{\text{pyr}} + \mu_{\text{oct}}^2 N_{\text{oct}} + \mu_{\text{dim}}^2 N_{\text{dim}}, \quad (1)$$

where N_{Ir} is the total number of Ir sites, and $N_{\text{pyr}} = 1$, $N_{\text{oct}} = 2$, and $N_{\text{dim}} = 6$ are, respectively, the numbers of sites for Ir⁴⁺ in triangular pyramid, Ir⁵⁺ in octahedra, and Ir⁵⁺ in dimer. If as predicted octahedrally coordinated Ir⁵⁺ is in a spin-orbit coupled nonmagnetic state [4], all the magnetic moments deduced from the Curie constant must be assigned to the Ir⁴⁺ ions on the Ir2 site. This would lead to a rather large effective moment of 6.15 μ_{B} . This value is only slightly reduced by adopting the more likely literature values for Ir⁵⁺ discussed above. For instance, when 0.2 μ_{B}/Ir for the dimers [7] and 0.91 μ_{B}/Ir for the regular octahedra [6] are used, the moment expected for each Ir⁴⁺ becomes 6.0 μ_{B} , which is still fairly large. Interestingly it is close to the expected value of 5.9 μ_{B} for the state $S = 5/2$.

To the best of our knowledge, Ir⁴⁺ within the triangular pyramid environment has not yet been reported or considered theoretically. Our preliminary *ab initio* many-body configuration interaction calculations [34] on the IrO₄ unit, performed to understand the electronic multiplet structure of the Ir⁴⁺ ion at the Ir2 site, indicate an orbitally nondegenerate low-spin ground state. As a result, the spin-orbit coupling in the 5d Ir atom, though strong, has little effect on the ground state—less than 20% contribution from the excited orbital states. However, a distortion, e.g., the Ir⁴⁺ atom moving towards the tetrahedral position of the triangular pyramid, could help result in the high-spin $S = 5/2$ ground state. In fact, our calculations on an ideal IrO₄ tetrahedra with Ir-O bond lengths of 1.9 Å (\approx average of the Ir-O bond lengths at the Ir2 site) show that the ⁶A₁ ($S = 5/2$) state is rather close, ~ 0.33 eV, to the low-spin ²T₂ ground state of the tetrahedral point group symmetry. The high-spin state could then be stabilized by further distortion, interactions, or other correlated effects, which we leave for future work.

We thank P. Huang and P. Babkevich for helpful discussions. This work was supported by the Swiss National Science Foundation, its Sinergia network MPBH, and a European Research Council grant (CONQUEST). M.J. is grateful for support by the European Commission through the Marie Skłodowska-Curie Action COFUND (EPFL Fellows).

-
- [1] W. Witzczak-Krempa, G. Chen, Y. B. Kim, and L. Balents, *Annu. Rev. Condens. Matter Phys.* **5**, 57 (2014).
[2] D. A. Pesin and L. Balents, *Nat. Phys.* **6**, 376 (2010).
[3] J. G. Rau, E. K.-H. Lee, and H.-Y. Kee, *Annu. Rev. Condens. Matter Phys.* **7**, 195 (2016).
[4] D. I. Khomskii, *Transition Metal Compounds*, (Cambridge University, Cambridge, England, 2014).
[5] T. Dey, A. Maljuk, D. V. Efremov, O. Kataeva, S. Gass, C. G. F. Blum, F. Steckel, D. Gruner, T. Ritschel, A. U. B. Wolter, J. Geck, C. Hess, K. Koepernik, J. van den Brink, S. Wurmehl, and B. Büchner, *Phys. Rev. B* **93**, 014434 (2016).
[6] G. Cao, T. F. Qi, L. Li, J. Terzic, S. J. Yuan, L. E. DeLong, G. Murthy, and R. K. Kaul, *Phys. Rev. Lett.* **112**, 056402 (2014).
[7] A. Nag, S. Middey, S. Bhowal, S. K. Panda, R. Mathieu, J. C. Orain, F. Bert, P. Mendels, P. G. Freeman, M. Mansson, H. M. Rønnow, M. Telling, P. K. Biswas, D. Sheptyakov, S. D. Kaushik, Vasudeva Siruguri, C. Meneghini, D. D. Sarma, I. Dasgupta, and S. Ray, *Phys. Rev. Lett.* **116**, 097205 (2016).
[8] G. Cao, J. Bolivar, S. McCall, J. E. Crow, and R. P. Guertin, *Phys. Rev. B* **57**, R11039 (1998).
[9] B. J. Kim, H. Jin, S. J. Moon, J.-Y. Kim, B.-G. Park, C. S. Leem, Jaejun Yu, T. W. Noh, C. Kim, S.-J. Oh, J.-H. Park, V. Durairaj, G. Cao, and E. Rotenberg, *Phys. Rev. Lett.* **101**, 076402 (2008).
[10] B. J. Kim, H. Ohsumi, T. Komesu, S. Sakai, T. Morita, H. Takagi, and T. Arima, *Science* **323**, 1329 (2009).
[11] V. M. Katukuri, V. Yushankhai, L. Siurakshina, J. van den Brink, L. Hozoi, and I. Rousochatzakis, *Phys. Rev. X* **4**, 021051 (2014).
[12] J. G. Vale, S. Boseggia, H. C. Walker, R. Springell, Z. Feng, E. C. Hunter, R. S. Perry, D. Prabhakaran, A. T. Boothroyd, S. P. Collins, H. M. Rønnow, and D. F. McMorrow, *Phys. Rev. B* **92**, 020406(R) (2015).

- [13] S. Boseggia, H. C. Walker, J. Vale, R. Springell, Z. Feng, R. S. Perry, M. Moretti Sala, H. M. Rønnow, S. P. Collins, and D. F. McMorrow, *J. Phys. Condens. Matter* **25**, 422202 (2013).
- [14] M. Moretti Sala, V. Schnell, S. Boseggia, L. Simonelli, A. Al-Zein, J. G. Vale, L. Paolasini, E. C. Hunter, R. S. Perry, D. Prabhakaran, A. T. Boothroyd, M. Krisch, G. Monaco, H. M. Rønnow, D. F. McMorrow, and F. Mila, *Phys. Rev. B* **92**, 024405 (2015).
- [15] P. Gegenwart and S. Trebst, *Nat. Phys.* **11**, 444 (2015).
- [16] D. Uematsu, H. Sagayama, T. H. Arima, J. J. Ishikawa, S. Nakatsuji, H. Takagi, M. Yoshida, J. Mizuki, and K. Ishii, *Phys. Rev. B* **92**, 094405 (2015).
- [17] L. Hozoi, H. Gretarsson, J. P. Clancy, B.-G. Jeon, B. Lee, K. H. Kim, V. Yushankhai, P. Fulde, D. Casa, T. Gog, J. Kim, A. H. Said, M. H. Upton, Y.-J. Kim, and J. van den Brink, *Phys. Rev. B* **89**, 115111 (2014).
- [18] S. Kanungo, B. Yan, P. Merz, C. Felser, and M. Jansen, *Angew. Chem.* **127**, 5507 (2015).
- [19] A. J. M. Duisenberg, L. M. J. Kroon-Batenburg, and A. M. M. Schreurs, *J. Appl. Crystallogr.* **36**, 220 (2003).
- [20] G. Oszlányi and A. Sütö, *Acta Crystallogr., Sect. A* **60**, 134 (2004).
- [21] V. Petricek, M. Dusek, and L. Palatinus, *Z. Kristallogr.* **229**, 345 (2014).
- [22] See Supplemental Material at <http://link.aps.org/supplemental/10.1103/PhysRevB.94.104403> for details on crystallographic data, results of Seebeck coefficient measurements, and details on valence configurations.
- [23] Y. Doi and Y. Hinatsu, *J. Phys.: Condens. Matter* **16**, 2849 (2004).
- [24] R. D. Burbank and H. T. Evans, *Acta Crystallogr.* **1**, 330 (1948).
- [25] G. Cao, Y. Xin, C. S. Alexander, J. E. Crow, P. Schlottmann, M. K. Crawford, R. L. Harlow, and W. Marshall, *Phys. Rev. B* **66**, 214412 (2002).
- [26] M. Bremholma, S. E. Duttona, P. W. Stephensb, and R. J. Cava, *J. Solid State Chem.* **184**, 601 (2011).
- [27] M. Jenderka, J. Barzola-Quiquia, Z. P. Zhang, H. Frenzel, M. Grundmann, and M. Lorenz, *Phys. Rev. B* **88**, 045111 (2013).
- [28] H. Okabe, M. Isobe, E. Takayama-Muromachi, N. Takeshita, and J. Akimitsu, *Phys. Rev. B* **88**, 075137 (2013).
- [29] C. Lu, A. Quindeau, H. Deniz, D. Preziosi, D. Hesse, and M. Alexe, *Appl. Phys. Lett.* **105**, 082407 (2014).
- [30] F. C. Chou, J. H. Cho, and Y. S. Lee, *Phys. Rev. B* **70**, 144526 (2004).
- [31] L. Yang, A. Pisoni, A. Magrez, S. Katrych, A. Arakcheeva, B. Dalla Piazza, K. Prša, J. Jaćimović, A. Akrap, J. Teyssier, L. Forró, and H. M. Rønnow, *Inorg. Chem.* **54**, 4371 (2015).
- [32] T. Sakamoto, Y. Doi, and Y. Hinatsu, *J. Solid State Chem.* **179**, 2595 (2006).
- [33] For both the Ir1 and Ir3 octahedral units in combination B, each Ir⁵⁺ ions are surrounded by six O²⁻ ions so that the total charge ($Q_{\text{oct}}^{\text{B}}$) sums up as $5 + 6 \times (-2) = -7$. Likewise, for the Ir2 triangular pyramidal unit, each Ir⁴⁺ ion surrounded by four O²⁻ ions provides the total charge ($Q_{\text{pyr}}^{\text{B}}$) of $4 + 4 \times (-2) = -4$.
- [34] V. M. Katukuri, H. Stoll, J. van den Brink, and L. Hozoi, *Phys. Rev. B* **85**, 220402(R) (2012).